Surfaces and Interfaces 87 (2026) 108930

Contents lists available at ScienceDirect

Surfaces and Interfaces

journal homepage: www.sciencedirect.com/journal/surfaces-and-interfaces

ZnO: Cu/FTO/Ag nano-heterostructure arrays as the sensitive, stable, and multifunctional surface-enhanced Raman scattering substrates

Tung-Hao Chang [a], Yu-Fan Chen [b], Yang-Chun Lee [c], Yu-Cheng Chang [b,*]

[a] Department of Radiation Oncology, Changhua Christian Hospital, Changhua, 50006, Taiwan
[b] Department of Materials Science and Engineering, Feng Chia University, Taichung, 40724, Taiwan
[c] Department of Electronic and Computer Engineering, National Taiwan University of Science and Technology, Taipei 10607, Taiwan

ARTICLE INFO

Keywords:
Surface-enhanced Raman scattering
Fluorine-doped tin oxide
Ag nanoparticles
Finite-difference time-domain
Rhodamine 6 G
Amoxicillin

ABSTRACT

A novel 3D hierarchical surface-enhanced Raman scattering (SERS) platform was engineered, in which the strategic insertion of a 5.5 nm fluorine-doped tin oxide (FTO) interlayer between ZnO: Cu nanoneedle arrays and Ag nanoparticles proved critical for achieving ultra-sensitivity. The ZnO: Cu/FTO/Ag nano-heterostructure arrays were systematically optimized, demonstrating a powerful dual-enhancement mechanism. Finite-difference time-domain (FDTD) simulations and experimental data confirmed that the FTO layer simultaneously facilitates interfacial charge transfer and amplifies 'hotspot' intensity by optimizing plasmonic coupling. This synergistic design delivered an outstanding enhancement factor (EF) of 5.95×10^8 (a 1.42-fold increase over the non-FTO control). Notably, the platform achieved an exceptional femtomolar (fM)-level limit of detection for rhodamine 6 G (1 fM)—a 1000-fold improvement—and detected the antibiotic amoxicillin at a concentration as low as 10 picomolar (pM). Furthermore, the FTO interlayer provided superior 21-day storage stability (acting as a protective barrier), excellent spot-to-spot uniformity, and robust photocatalytic reusability. This work validates an effective design strategy for engineering highly stable and ultra-sensitive SERS sensors for practical trace-level diagnostics.

1. Introduction

Surface-enhanced Raman scattering (SERS) stands as an exceptionally versatile and powerful analytical technique that dramatically amplifies the Raman signal of molecules adsorbed onto metallic nanostructures [1,2]. This remarkable amplification has catapulted SERS to the forefront as a highly sensitive and promising analytical tool across a wide array of disciplines, including chemistry, biology, environmental science, pharmaceuticals, and clinical diagnostics [3,4]. One of SERS's hallmark advantages is its non-destructive nature, enabling the extraction of invaluable molecular structural information without compromising sample integrity [5,6]. The extraordinary enhancement effect in SERS is principally attributed to two distinct yet synergistic mechanisms [7,8]. The first is the electromagnetic (EM) enhancement mechanism, driven by the excitation of localized surface plasmon resonances (LSPRs) on noble metal surfaces [9]. This phenomenon results in a massive amplification of the local electric field, capable of providing an enhancement factor of up to 10^6 [10,11]. For the EM mechanism, the morphology and distribution of the noble metal nanostructures within SERS substrates are critical parameters that can be precisely engineered by manipulating their size and placement on suitable supporting materials [12–14]. The second mechanism, chemical (CM) enhancement, arises from charge transfer between the adsorbed molecule and the substrate surface, which significantly enhances the molecular polarizability tensor and, consequently, the Raman signal [15,16]. Despite its immense potential, the practical fabrication of optimized SERS substrates remains a challenge [17]. These include achieving high nanostructure density, preventing uncontrolled nanoparticle aggregation, and ensuring uniform distribution of these nanostructures across the substrate surface [18,19]. Addressing these challenges is crucial for unlocking the full potential of SERS for widespread, reliable analytical applications.

To overcome these limitations, semiconductor/noble metal heterostructures have emerged as a class of exceptionally promising substrates for SERS, enabling ultrasensitive and highly reproducible molecular detection [20,21]. These advanced platforms leverage a synergistic interplay between semiconductor and noble metal components, resulting in enhanced physicochemical properties, unique surface wetting for

* Corresponding author.
E-mail address: yuchchang@fcu.edu.tw (Y.-C. Chang).

https://doi.org/10.1016/j.surfin.2026.108930
Received 5 February 2026; Received in revised form 25 February 2026; Accepted 4 March 2026
Available online 5 March 2026
2468-0230/© 2026 Elsevier B.V. All rights are reserved, including those for text and data mining, AI training, and similar technologies.

efficient molecular adsorption, consistent and reliable SERS signals that are robust against photochemical reactions, and an inherent self-cleaning capability [22,23]. A broad spectrum of semiconductor/noble metal heterostructures has been successfully explored as high-performance SERS platforms, including notable examples like TiO_2/Ag [24,25], ZnO/Ag [26–28], Si/Ag [29,30], SiO_2/Ag [31,32], and Ge/Ag [33]. Among these, one-dimensional (1D) ZnO nanostructures decorated with noble metal nanoparticles have recently garnered significant attention as SERS substrates due to their exceptional detection sensitivity, stability, uniformity, and biocompatibility [21,26]. Moreover, a discernible trend in the field highlights a growing preference for precisely engineered ternary heterostructures over their binary counterparts for even more refined SERS applications [34–36].

Concurrently, fluorine-doped tin oxide (FTO) has garnered significant attention as a highly attractive substrate material, owing to an impressive portfolio of advantageous properties, including remarkable stability under atmospheric conditions, chemical inertness, high-temperature resistance, and excellent resistance to physical wear [37,38]. The foundational material, tin dioxide (SnO_2), inherently possesses a stable tetragonal rutile structure and is classified as an n-type semiconductor [39,40]. To further enhance its optical and electrical characteristics, tin dioxide is frequently doped with various elements or chemicals [41,42]. When fluorine is incorporated as the dopant, FTO exhibits a range of desirable traits: high visible-light transmittance, an increased ultraviolet absorption coefficient, significantly reduced surface resistivity, enhanced chemical stability, and robust resistance to acids and alkalis at room temperature [43,44]. These compelling attributes have catalyzed the widespread adoption of FTO across diverse fields, including thin-film solar cells, dye-sensitized solar cells (DSSCs), perovskite solar cells, touchscreens, various optical devices, liquid crystal displays (LCDs), organic light-emitting diodes (OLEDs), and biosensors [45–53]. In transparent electrode applications, FTO is recognized as one of the most widely studied and well-established materials [54,55]. Despite its versatility and widespread use, a comprehensive literature survey reveals a notable research gap: the direct fabrication and utilization of decorated FTO thin films containing silver (Ag) nanoparticles on zinc oxide (ZnO) nanostructures for SERS applications have not yet been explored. This unexplored territory presents a compelling opportunity for innovation in the development of advanced SERS substrates.

Herein, we address this gap by presenting a facile and scalable approach for the rational design and fabrication of three-dimensional ZnO: Cu/FTO/Ag nano-heterostructures directly on glass substrates. This method leverages a synergistic combination of simple wet chemical synthesis and sputtering techniques. This strategic hybrid approach yields heterostructures with outstanding homogeneity, large-area uniformity, and high reproducibility—all pivotal factors for maximizing SERS signal enhancement. Critically, the as-developed Cu-doped ZnO/FTO/Ag nano-heterostructures function as a superior SERS substrate, enabling the ultra-sensitive detection of diverse chemical analytes. This capability is exemplified by the remarkable detection limits achieved for rhodamine 6 G (1 fM) and the antibiotic amoxicillin (10 pM). These results underscore the significant potential of these platforms for highly sensitive and reliable chemical sensing applications, paving the way for the further development of advanced FTO-based SERS systems.

2. Experimental

2.1. Fabrication of the ZnO: Cu/FTO/Ag nano-heterostructure arrays

A schematic illustration of the fabrication protocol for the ZnO: Cu/FTO/Ag nano-heterostructure arrays is shown in Fig. 1. The procedure began with the deposition of a thin ZnO seed layer onto meticulously cleaned glass substrates via spin coating. A subsequent thermal annealing step was employed to enhance the crystallinity and adhesion of the seed layer [56]. Next, vertically aligned ZnO: Cu nanoneedle arrays were grown using a facile wet-chemical method. The ZnO: Cu precursor solution was prepared by dissolving zinc nitrate hexahydrate, hexamethylenetetramine, 1,3-diaminopropane, and copper(II) chloride dihydrate in 100 mL of deionized (DI) water, maintaining a precise molar ratio of 1:1:12:0.23, respectively. To investigate the influence of precursor concentration on the resulting morphology, this solution was prepared at several different total concentrations. The seeded substrates were then vertically immersed in the prepared solution in a 150-mL crystallization dish and held at 90 °C for 3 h. After the growth process, the samples were rigorously rinsed with DI water and ethanol, then dried at 70 °C for 1 h. Subsequently, a conductive FTO layer was deposited on the as-synthesized ZnO: Cu nanoneedles using radio-frequency (RF) magnetron sputtering at room temperature; the film's properties were modulated by varying the deposition time. In the final step, silver (Ag) nanoparticles were deposited onto either the pristine ZnO: Cu nanoneedles or the as-prepared ZnO: Cu/FTO heterostructures. This process was conducted via direct current (DC) magnetron sputtering, also at room temperature.

2.2. Materials characterization

The morphological, structural, and compositional characteristics of

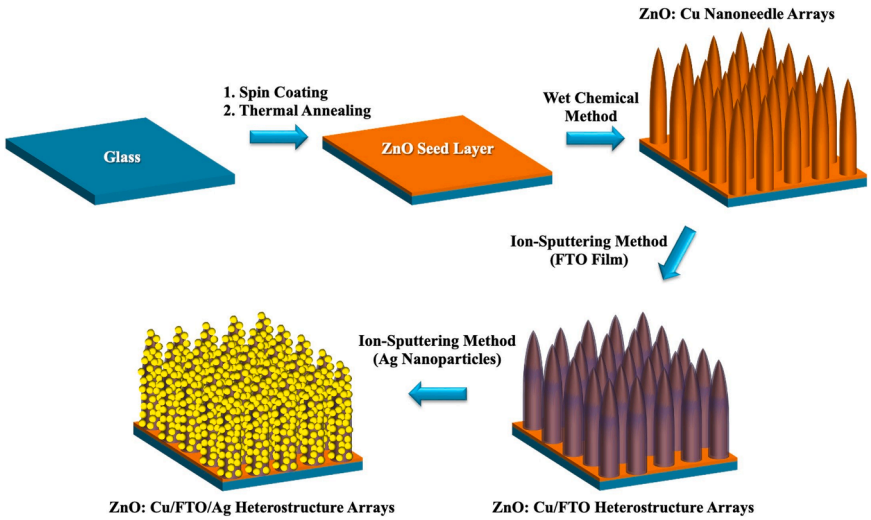


Fig. 1. Schematic depicting the step-by-step fabrication of the ZnO: Cu/FTO/Ag nano-heterostructure arrays.

the as-fabricated SERS substrates were systematically evaluated using a suite of characterization techniques. The surface morphology and microstructure were analyzed using field-emission scanning electron microscopy (FESEM; Hitachi S-4800, Japan) and field-emission transmission electron microscopy (FETEM; JEOL-2100F, Japan). The latter instrument was equipped with an energy-dispersive X-ray spectroscopy (EDS) detector for comprehensive elemental analysis and mapping. The crystalline phase and structure of the ZnO: Cu nanoneedle arrays were ascertained by X-ray diffraction (XRD; Bruker D8 SSS, United States). Furthermore, the surface chemical states and elemental compositions were investigated via X-ray photoelectron spectroscopy (XPS; ULVAC-PHI 5000 VersaProbe, Japan).

2.3. SERS detection and theoretical simulations

To assess the SERS activity of the ZnO: Cu/FTO/Ag nanoheterostructures, rhodamine 6 G (R6G) and amoxicillin were utilized as model probe molecules, representing a chemical dye and an antibiotic analyte, respectively. For sample preparation, the as-prepared SERS substrates were immersed in aqueous solutions containing the analytes at various concentrations for 1 h at room temperature, followed by drying under a gentle stream of nitrogen. All SERS spectra were acquired using a micro-Raman spectrometer (MRI532S; Protrustech, Taiwan) operating with a 532 nm excitation laser. The system was configured with a 3.3 mm laser beam diameter and a spectral resolution of 2.2 cm^{-1}. The SERS enhancement factor (EF) of the substrate was calculated according to the established equation: $EF = (I_{SERS} \times C_R) / (I_R \times C_{SERS})$, where I_{SERS} and I_R denote the intensities of the characteristic R6G peak at 1648 cm^{-1} obtained from the SERS and conventional Raman spectra, respectively. In this context, C_{SERS} and C_R represent the respective molar concentrations of the analyte used for the SERS and reference Raman measurements. Furthermore, to provide theoretical insight into the enhancement mechanism, the three-dimensional finite-difference time-domain (3D-FDTD) method was employed to simulate the local electric field distribution on the surface of the ZnO: Cu/FTO/Ag nanoheterostructures within different dielectric environments.

3. Results and discussion

3.1. Fabrication and characterization of the ZnO: Cu/FTO/Ag nanoheterostructure arrays

Fig. 2a–f present a series of FESEM images illustrating the morphological evolution of ZnO: Cu nanoneedle arrays synthesized via the wet-chemical method. As previously detailed, the precursor solution was formulated using zinc nitrate hexahydrate, hexamethylenetetramine, 1,3-diaminopropane, and copper(II) chloride dihydrate, with a fixed molar ratio of 1:1:12:0.23, respectively. The influence of total precursor concentration was systematically investigated at 2.5, 5, 10, 20, 30, and 40 mM. As observed in Fig. 2, vertically aligned ZnO: Cu nanoneedle arrays were successfully fabricated on the ZnO-seeded glass substrates. A distinct trend emerged in which the nanoneedle diameter systematically increased with increasing precursor concentration. Specifically, the average diameters were ascertained as 81.5 nm (2.5 mM), 98.4 nm (5 mM), 117.6 nm (10 mM), 147.7 nm (20 mM), 150.8 nm (30 mM), and 180.2 nm (40 mM). Conversely, nanoneedle density generally decreased with increasing precursor concentration, with average values of 61 (2.5 mM), 48 (5 mM), 36 (10 mM), 43 (20 mM), 18 (30 mM), and 9 μm^{-2} (40 mM). These findings clearly indicate that an elevated precursor concentration promotes the radial growth of the nanoneedles while concurrently diminishing their surface density. Notably, the nanoneedles reached their maximum diameter and exhibited the sparsest distribution at the highest concentration of 40 mM. Furthermore, as shown in Fig. S1 a–f, the average nanoneedle length increased progressively with increasing precursor concentration. The approximate lengths were recorded as 2.5, 3.5, 7, 10, 11.5, and 13.5 μm for the corresponding concentrations of 2.5, 5, 10, 20, 30, and 40 mM, respectively (Fig. S1g). This systematic elongation with increasing precursor levels reinforces the observed morphological evolution, providing crucial insights into the mechanisms governing the controlled anisotropic growth of ZnO: Cu nanostructures across varied chemical environments.

Fig. 3a displays the X-ray diffraction (XRD) pattern for the ZnO: Cu nanoneedle arrays synthesized using a 20 mM precursor concentration. The prominent diffraction peaks observed at 2 theta values of 34.59° and 72.74° are unambiguously attributed to the (002) and (004) planes of hexagonal wurtzite ZnO (JCPDS card no 36-1451), respectively. These sharp and distinct peaks provide strong evidence that the ZnO: Cu nanoneedles exhibit a preferential growth orientation along the [001] crystallographic direction. As highlighted in the inset of Fig. 3a, a subtle yet significant shift of the (002) peak to 34.59° from 34.55° (typical for undoped ZnO) is observed. This shift is attributed to lattice compression induced by the substitutional incorporation of smaller Cu^{2+} ions (ionic radius: 0.073 nm) replacing larger Zn^{2+} ions (ionic radius: 0.074 nm) within the ZnO crystal lattice. To corroborate successful doping and further analyze the surface chemistry, X-ray photoelectron spectroscopy (XPS) was performed. The full XPS survey spectrum of the ZnO: Cu nanoneedle arrays (Fig. 3b) unequivocally confirms the presence of Zn, O, and Cu elements on the sample's surface. In the inset of Fig. 3b, the high-resolution Cu 2p spectrum reveals two characteristic peaks at binding energies of 932.9 eV and 952.6 eV, corresponding to the Cu $2p_{3/2}$ and Cu $2p_{1/2}$ spin-orbit doublet, respectively [57,58]. Collectively,

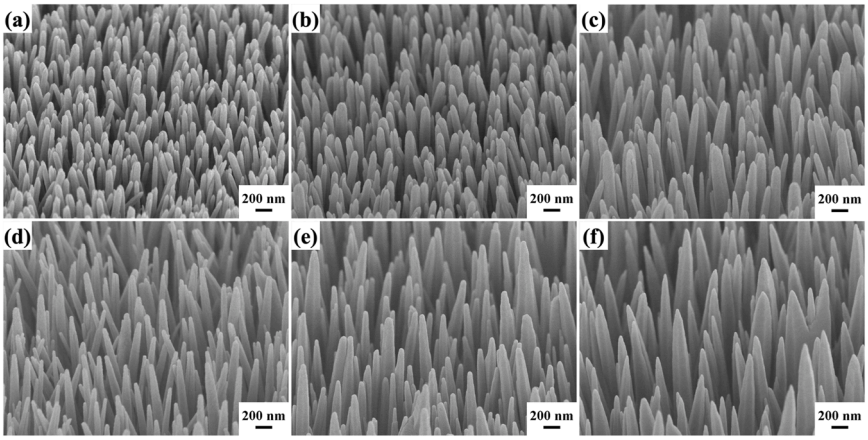


Fig. 2. The tilt-view FESEM images of ZnO: Cu nanoneedle arrays grown at the different precursor concentrations. The precursor concentrations are (a) 2.5, (b) 5, (c) 10, (d) 20, (e) 30, and (f) 40 mM, respectively.

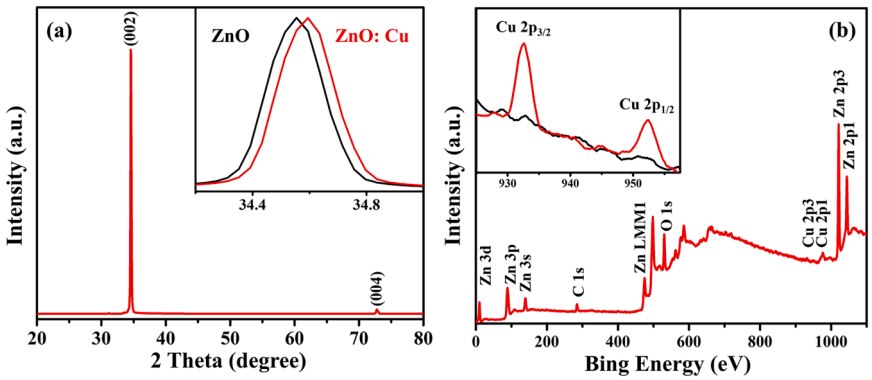


Fig. 3. (a) XRD spectrum of ZnO: Cu nanoneedle arrays (20 mM precursor). The inset XRD spectra are slow-scan scans of the [002] peaks for the ZnO and ZnO: Cu nanoneedle arrays (20 mM precursor). (b) XPS survey spectrum of ZnO: Cu nanoneedle arrays (20 mM precursor). The inset XPS spectra Cu 2p spectra of ZnO and ZnO: Cu nanoneedle arrays (20 mM precursor).

these crystallographic and spectroscopic findings provide robust evidence for the successful incorporation of Cu into the ZnO lattice, thereby confirming the synthesis of phase-pure ZnO: Cu nanoneedles.

The highly ordered ZnO: Cu nanoneedle arrays served as an ideal three-dimensional template for the subsequent deposition of Ag nanoparticles via ion sputtering, resulting in the formation of ZnO: Cu/Ag nano-heterostructure arrays. Fig. 4a–e display FESEM backscattered electron images (BEIs) that illustrate the distribution of Ag nanoparticles on the ZnO: Cu nanoneedles (synthesized using a 20 mM ZnO: Cu precursor) as a function of varying direct current (DC) sputtering times. As the sputtering time increased, a clear progression was observed, characterized by a systematic increase in both the size and surface coverage density of the Ag nanoparticles. Notably, complete surface coverage with Ag nanoparticles was achieved after 1 min of sputtering. However, prolonged sputtering beyond this point led to undesirable aggregation of Ag nanoparticles into larger clusters or, potentially, the formation of a continuous Ag layer, a morphology known to be detrimental to the local surface electric field enhancement required for optimal SERS activity. A further investigation into the detailed morphology and crystalline structure of the ZnO: Cu/Ag nano-heterostructures (specifically those prepared with a 1-minute DC sputtering time) was performed using field-emission transmission electron microscopy (FETEM) analyses, as depicted in Fig. S2a and b. Both low- and high-magnification FETEM images clearly confirmed the uniform decoration of Ag nanoparticles across the ZnO: Cu nanoneedle surfaces. Furthermore, the high-resolution TEM (HRTEM) image (Fig. S2c) revealed lattice spacings of 0.262 nm and 0.238 nm, corresponding to the (002) plane of hexagonal ZnO (JCPDS no 36-1451) and the (111) plane of cubic Ag (JCPDS no 65-2871), respectively. This finding provides direct, compelling evidence for the successful formation of the ZnO: Cu/Ag nano-heterostructure. The elemental distribution was thoroughly probed using energy-dispersive X-ray spectroscopy (EDS) elemental mapping (Fig. S2d), which confirmed the uniform presence of Zn, O, Cu, and Ag throughout the nanostructure. The corresponding EDS spectrum (Fig. S2e) further corroborated the detection of these elements; the minor Au signal observed was attributed solely to the TEM grid material. Crucially, the absence of other detectable impurity signals confirmed the high phase purity of the synthesized ZnO: Cu/Ag nano-heterostructure.

The morphological evolution of FTO coatings deposited onto ZnO: Cu nanoneedle arrays was systematically investigated as a function of radio-frequency (RF) magnetron sputtering time. Fig. S3 a–f present FESEM micrographs of ZnO: Cu nanoneedle arrays (20 mM precursor concentration) after FTO deposition for sputtering times of 0.5, 1, 2, 3, 5, and 7 min. As the sputtering duration increased, a clear trend emerged, characterized by a progressive increase in both the surface coverage and the FTO layer thickness. This progressive FTO deposition caused the nanoneedles to appear significantly thicker, and the interspacing between adjacent structures diminished due to their partial encapsulation by the growing FTO film. To conduct a more detailed nanoscale structural analysis, FETEM was employed. Fig. 5a shows a representative low-magnification FETEM image of a ZnO: Cu/FTO nano-heterostructure fabricated using a 1-minute RF sputtering duration. High-resolution TEM images (Fig. 5b and c) clearly reveal a uniform, amorphous layer with an approximate thickness of 5.5 nm that conformally coats the nanoneedle surface, which is unambiguously identified as the sputtered FTO coating. Crucially, the underlying crystalline

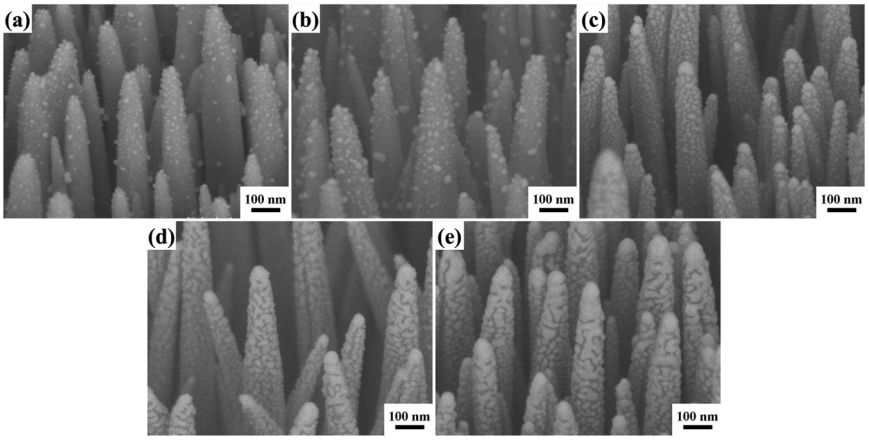


Fig. 4. The tilt-view FESEM BEIs of ZnO: Cu/Ag nano-heterostructure arrays (20 mM precursor) with different Ag-sputtering times. The Ag-sputtering times are (a) 0.25, (b) 0.5, (c) 1, (d) 1.5, and (e) 2 min, respectively.

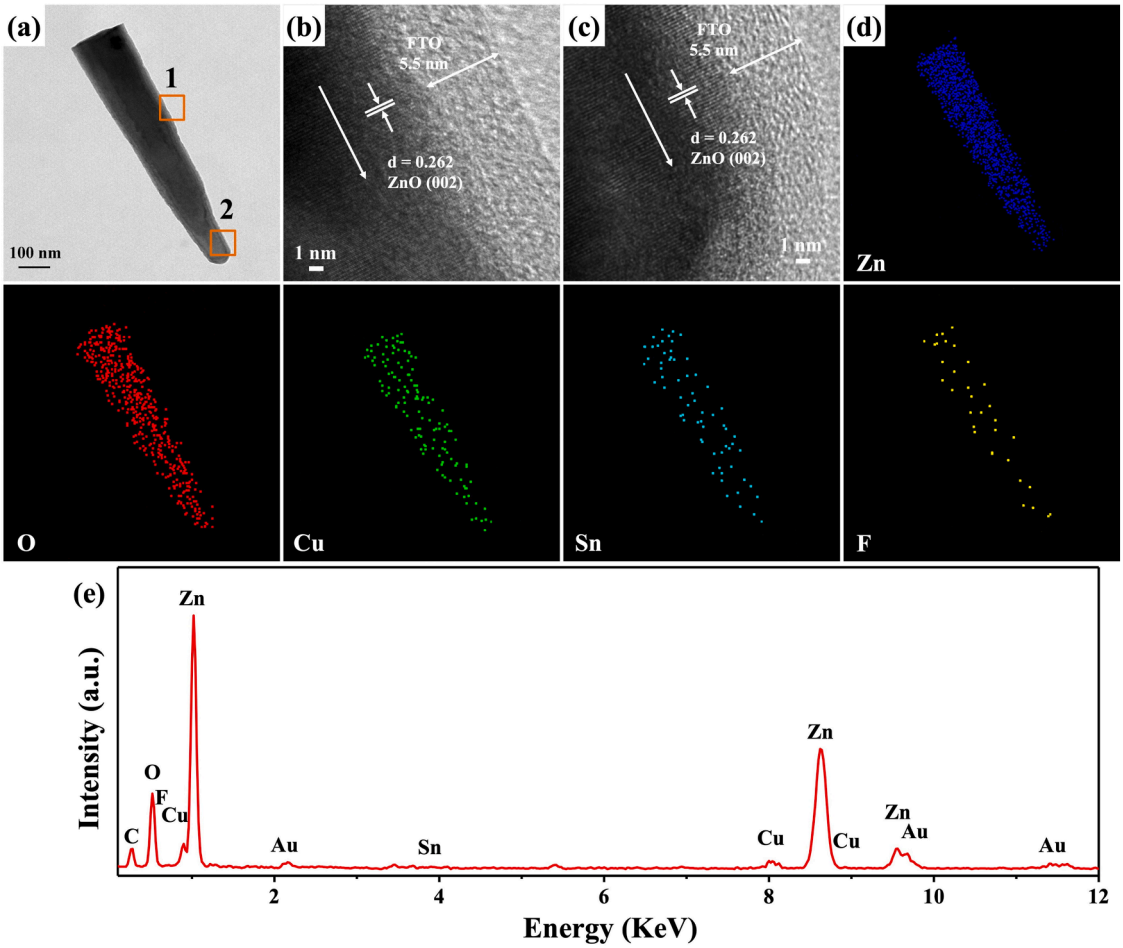


Fig. 5. (a) TEM image, (b) HRTEM image (region 1), (c) HRTEM image (region 2), (d) EDS mapping images of a ZnO: Cu/FTO nano-heterostructure in Fig. 5a. The EDS mapping images of Zn, O, Cu, Sn, and F, respectively. (e) EDS spectrum of a ZnO: Cu/FTO nano-heterostructure.

ZnO: Cu core retained its structural integrity, exhibiting an interplanar spacing measured at 0.262 nm, corresponding to the (002) plane of hexagonal ZnO (JCPDS no 36-1451). This finding confirms the continued preferential orientation along the [001] axis despite the FTO deposition. To evaluate the elemental distribution within the ZnO: Cu/FTO heterostructures, energy-dispersive X-ray spectroscopy (EDS) mapping was performed. Fig. 5d provides a comprehensive elemental map, confirming the homogeneous distribution of Zn, O, Cu, Sn, and F, thereby validating the successful, uniform deposition of the FTO layer on the ZnO: Cu nanoneedles. The corresponding EDS spectrum (Fig. 5e) further corroborates this elemental composition, displaying distinct peaks attributable to each element. The absence of any extraneous signals underscores the high purity of the resulting ZnO: Cu/FTO nano-heterostructure.

The morphology and crystal structure of the optimal ZnO: Cu/FTO/Ag nano-heterostructure, fabricated with a 20 mM precursor concentration and 1-minute sputtering for both the FTO and Ag layers, were comprehensively characterized using FESEM and TEM. The tilt-view FESEM image (Fig. 6a) unequivocally demonstrates that the Ag nanoparticles form a dense and uniform coating encapsulating the underlying ZnO: Cu/FTO nano-heterostructure. A representative low-magnification FETEM image is presented in Fig. 6b. The HRTEM image (Fig. 6c) clearly reveals several key features: a conformal amorphous FTO layer with an approximate thickness of 5.5 nm, and distinct lattice fringes on an Ag nanoparticle with an interplanar spacing of 0.204 nm, corresponding to the (200) crystalline plane of cubic Ag (JCPDS no 65-2871). The XPS spectra of the ZnO: Cu/FTO/Ag nano-heterostructure (Fig. S4) reveal Ag $3d_{5/2}$ and Ag $3d_{3/2}$ peaks at 368.4 eV and 374.4 eV, respectively, confirming the presence of metallic silver in accordance with both literature values and HRTEM observations [59,60]. Fig. 6d displays the corresponding TEM-EDS elemental mapping analysis, confirming the homogeneous distribution of all constituent elements (Zn, O, Cu, Sn, F, and Ag), and visually verifying that the Ag is uniformly distributed across the entire surface of the ZnO: Cu/FTO nano-heterostructure. This elemental composition is further corroborated by the accompanying TEM-EDS spectrum (Fig. 6e).

3.2. SERS properties of ZnO: Cu/FTO/Ag nano-heterostructure arrays

Surface-enhanced Raman scattering (SERS) measurements were conducted at room temperature to systematically assess the SERS activity of the fabricated substrates. SERS is widely recognized for its high sensitivity, low detection limits, and excellent molecular selectivity [21,61,62]. The underlying enhancement mechanism is critically dependent on the type, morphology, and surface density of noble metal nanoparticles deposited on the substrate [30]. In this investigation, the influence of three key fabrication parameters on the final SERS performance was systematically optimized: the precursor concentration for ZnO: Cu nanoneedle growth and the sputtering durations for both the Ag nanoparticles and the FTO layers. The resulting Raman spectra are compiled in Fig. 7. Fig. 7a illustrates the SERS responses of ZnO: Cu nanoneedle arrays synthesized with varying precursor concentrations (2.5–40 mM), each subsequently decorated with Ag nanoparticles via a 1-minute sputtering process and probed by immersion in 10^{-6} M rhodamine 6 G (R6G) for 1 h. Among the tested configurations, the substrate prepared using a 20 mM precursor concentration yielded the

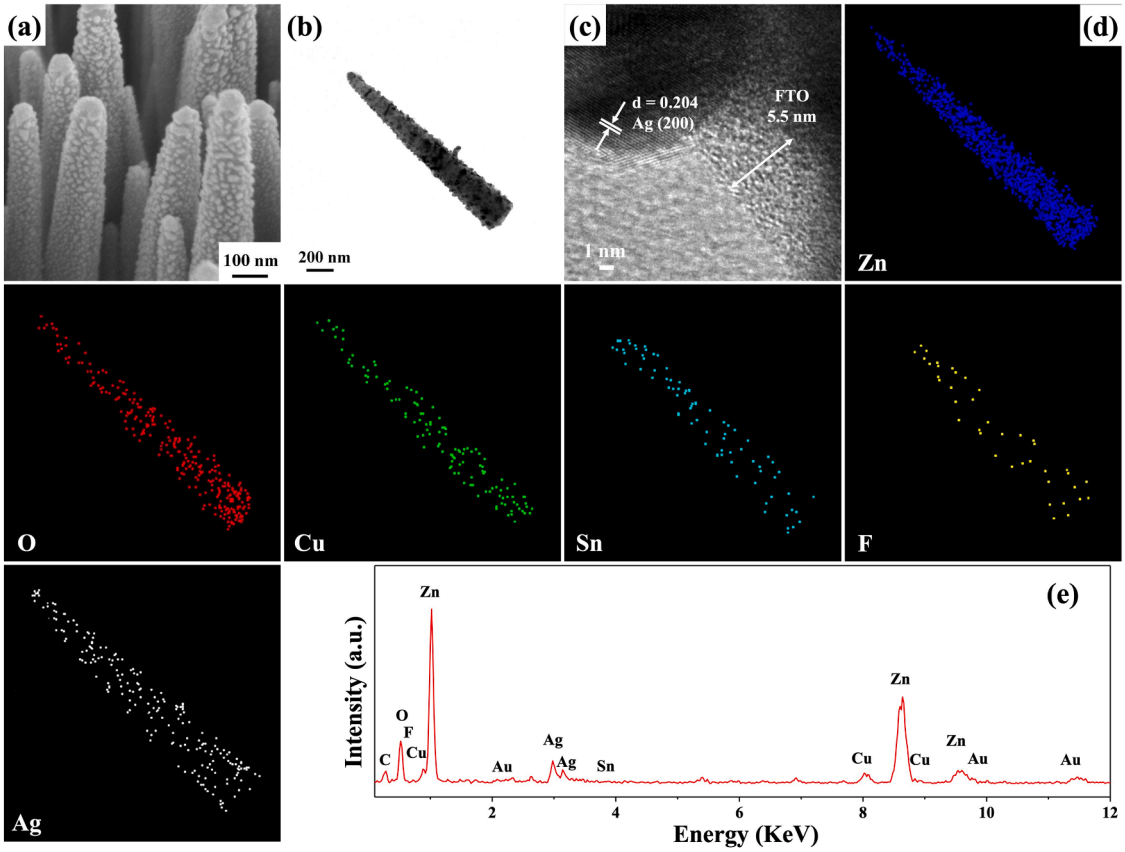


Fig. 6. (a) The tilt-view FESEM images of ZnO: Cu/FTO/Ag nano-heterostructure arrays (1 min FTO and 1 min Ag). (b) TEM image, (c) HRTEM image, (d) EDS mapping images of a ZnO: Cu/FTO/Ag nano-heterostructure in Fig. 7a. The EDS mapping images of Zn, O, Cu, Sn, F, and Ag, respectively. (e) EDS spectrum of a ZnO: Cu/FTO nano-heterostructure.

most intense Raman signal, indicating its superior enhancement capability. The effect of Ag sputtering duration on SERS performance was then evaluated (Fig. 7b). ZnO: Cu nanoneedle arrays (20 mM precursor concentration) were subjected to Ag deposition for varying durations (0.25 to 2 min). The Raman signal intensity peaked at a sputtering duration of 1 min, suggesting an optimal balance between the density of Ag nanoparticles and the generation of efficient plasmonic "hotspots." Fig. 7c presents the SERS spectra for substrates with different FTO sputtering durations (0.5–7 min), all of which were subsequently subjected to a fixed 1 min Ag nanoparticle deposition and immersion in 10^{-6} M R6G. The substrate fabricated with a 1-minute FTO sputtering time yielded the greatest Raman enhancement. This optimal performance is likely attributable to a favorable interface and enhanced charge-transfer synergy between the FTO layer and the deposited Ag nanoparticles. Collectively, these systematic optimization studies reveal that the ZnO: Cu/FTO/Ag nano-heterostructure—fabricated using a 20 mM ZnO: Cu precursor, a 1-minute FTO sputtering deposition, and a 1-minute Ag sputtering deposition—delivers the optimal SERS performance among all investigated configurations.

To validate the efficacy of the FTO layer as a superior intermediate layer for enhancing SERS activity in comparison to other materials, a comparative investigation was conducted. We fabricated analogous substrates with two distinct intermediate layers (ITO and Al_2O_3) between the ZnO:Cu nanoneedle arrays and the Ag nanoparticles. Crucially, an identical ion sputtering duration of 1 min was maintained for all intermediate layers. Fig. 8a displays the SERS spectra acquired from these composite substrates after immersion in a 10^{-6} M R6G solution for 1 h and subsequent air-drying. The results unequivocally demonstrate that the FTO intermediate layer yields the optimal SERS activity. Furthermore, the Surface-Enhanced Raman Scattering (SERS) enhancement factor (EF) values at 1648 cm^{-1} for the ZnO: Cu/Ag, ZnO: Cu/FTO/Ag, ZnO: Cu/ITO/Ag, and ZnO: Cu/Al_2O_3/Ag nano-heterostructure arrays were calculated to be 4.19×10^8, 5.95×10^8, 5.00×10^8, and 4.81×10^8, respectively. Notably, the SERS EF value for the ZnO: Cu/FTO/Ag nano-heterostructure is 1.42-fold higher than that of the ZnO: Cu/Ag nano-heterostructure (lacking an interlayer). Compared to the ZnO: Cu/Ag system, the ZnO: Cu/FTO/Ag nano-heterostructure features an FTO layer that more effectively facilitates electron-hole pair transfer, thereby further enhancing the SERS performance. This phenomenon is attributed to a synergistic Raman enhancement effect arising from interfacial charge-transfer mediated by the FTO layer, which amplifies overall SERS activity. Previous studies have indeed reported that metal-semiconductor hybrid structures can suppress electron-hole pair recombination, thereby significantly enhancing SERS performance [63–65].

The experimental findings clearly indicate that the ZnO: Cu/FTO/Ag nano-heterostructure arrays benefit substantially from the presence of the FTO interlayer, which is proposed to induce a synergistic Raman enhancement effect via interfacial charge transfer. To theoretically validate this assumption and elucidate the underlying enhancement mechanism—an essential step toward practical sensing applications—electromagnetic (EM) field simulations were conducted using the finite-difference time-domain (FDTD) method. These simulations modeled substrates with various intermediate layers under excitation at 532 nm, with the incident light propagating in the backward z-direction to replicate the laser illumination configuration used in the Raman measurements. As illustrated in Fig. 8b, the simulated electric field distributions reveal a pronounced geometric influence. Compared with the substrate lacking an interlayer, the incorporation of an intermediate layer significantly narrows the inter-particle gaps between adjacent Ag

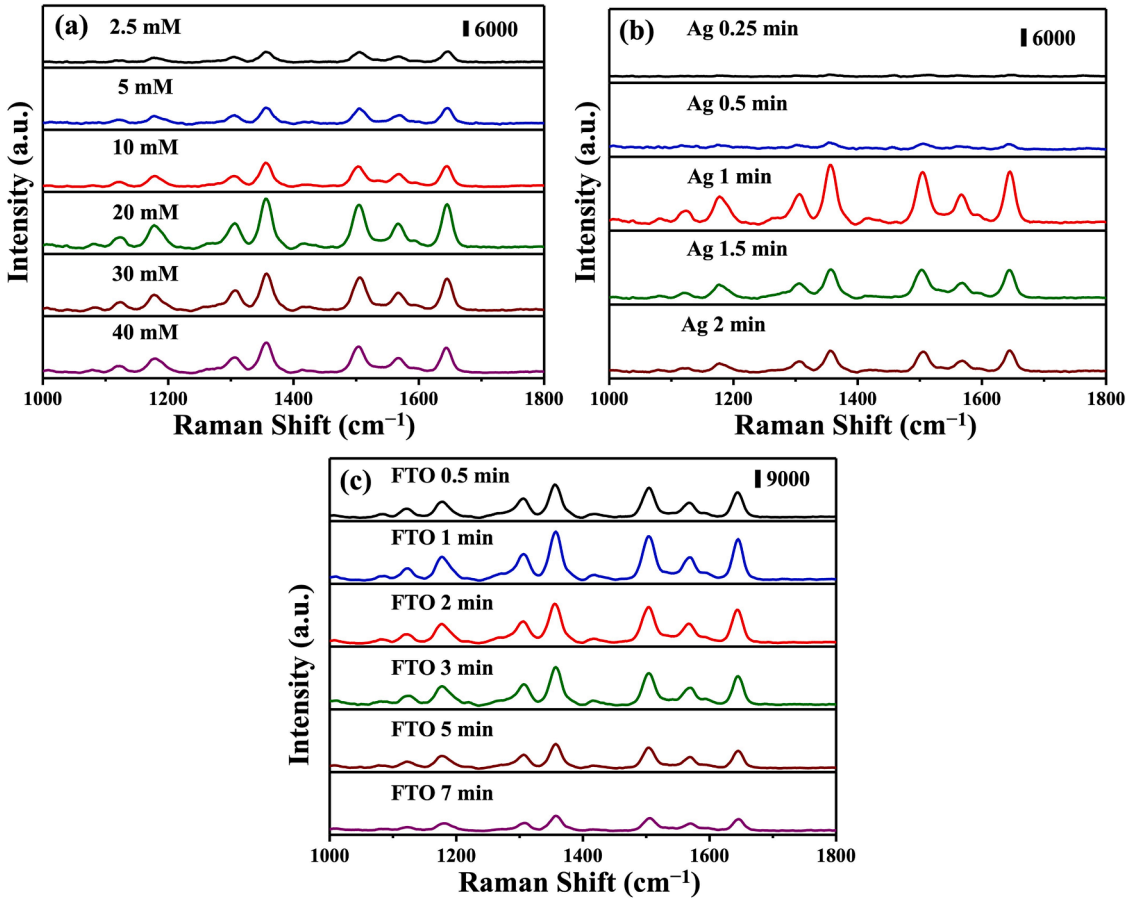


Fig. 7. (a) Raman spectra of R6G solution (10^{-6} M) from the ZnO: Cu/FTO/Ag nano-heterostructure arrays with the different concentrations of precursor (1 min Ag). (b) Raman spectra of R6G solution (10^{-6} M) from the ZnO: Cu/Ag nano-heterostructure arrays with different Ag-sputtering times. (c) Raman spectra of R6G solution (10^{-6} M) from the ZnO: Cu/FTO/Ag nano-heterostructure arrays with different FTO-sputtering times (1 min Ag).

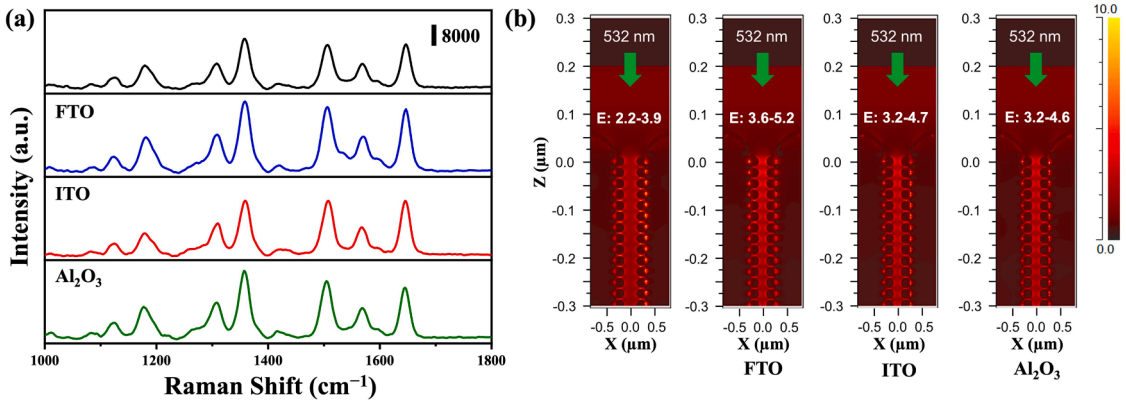


Fig. 8. (a) Raman spectra of R6G solution (10^{-6} M) and (b) simulated distributions of electromagnetic field intensity from the ZnO: Cu/Ag nano-heterostructure arrays with the different intermediate layer (at sputtering time of 1 min).

nanoparticles. This morphological change enhances plasmonic coupling, leading to a remarkable amplification of the local electric field, particularly in the so-called "hotspot" regions. Furthermore, the effect of the interlayer's dielectric properties was systematically examined. It was observed that increasing the refractive index of the interlayer weakens the field directly localized at the Ag/interlayer interface but concurrently strengthens the field within the hotspot junctions. This behavior can be attributed to the redistribution of plasmonic energy, as the electric field partially extends into the higher-index medium, thereby reducing confinement at the planar metal–dielectric interface. Such field delocalization enhances the electromagnetic intensity within the interparticle gaps, ultimately resulting in stronger localized surface plasmon resonance and more pronounced Raman signal amplification.

To evaluate a critical parameter for practical SERS applications, the signal uniformity of the fabricated substrates was investigated. Fig. 9a and b display the SERS spectra acquired from ten distinct, randomly selected locations on the ZnO: Cu/Ag and ZnO: Cu/FTO/Ag nano-heterostructure arrays, respectively, following immersion in 10^{-6} M R6G for 1 h. For both substrate types, the collected spectra show remarkable consistency in signal intensity across all 10 measured spots,

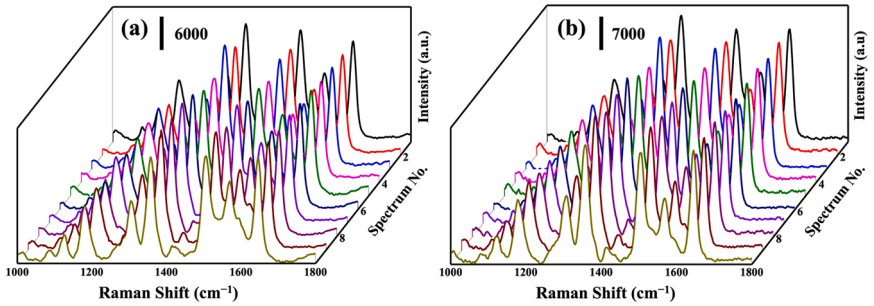


Fig. 9. Raman spectra of (10^{-6} M) R6G solution at 10 random points on (a) ZnO: Cu/Ag nano-heterostructure arrays and (b) ZnO: Cu/FTO/Ag nano-heterostructure arrays.

indicating excellent spatial uniformity of the SERS enhancement. Moreover, a visual comparison of the two figures clearly confirms that the ZnO: Cu/FTO/Ag nano-heterostructure arrays yield a substantially stronger Raman enhancement than the ZnO: Cu/Ag substrates. This result corroborates that the FTO interlayer plays a key role in augmenting the SERS response, an enhancement attributed to the previously discussed enhanced charge transfer mechanisms and a more favorable generation of plasmonic hotspots.

To assess practical viability, the reusability of the prepared SERS substrates was evaluated through five consecutive cycles of SERS detection (10^{-6} M R6G) followed by UV irradiation for photocatalytic regeneration. As illustrated in Fig. 10a and b for the ZnO: Cu/Ag and ZnO: Cu/FTO/Ag nano-heterostructure arrays, respectively, both substrate types exhibited exceptional robustness. Despite undergoing five repeated cycles, they maintained a remarkably stable Raman signal intensity, demonstrating outstanding reusability. This high degree of reusability is a critical attribute for practical and cost-effective SERS applications. Finally, the long-term storage stability of the substrates was assessed by monitoring their SERS performance against 10^{-6} M R6G over an extended 21-day period. Fig. 10c shows the Raman spectra recorded at designated time intervals, where each measurement was taken after a 1-hour immersion in the analyte solution. The ZnO: Cu/FTO/Ag nano-heterostructures demonstrated markedly superior stability, retaining a substantial level of Raman enhancement intensity for 21 days. This finding underscores the pivotal role of the sputter-deposited FTO layer, which not only amplifies the initial SERS signal but also critically enhances long-term operational stability, likely by acting as a protective encapsulating layer that mitigates oxidation or degradation of the underlying Ag nanoparticles.

To further probe the analytical sensitivity of the developed SERS substrates, their detection capabilities for trace concentrations of R6G solution were assessed. As detailed in Fig. 11a and b, the substrates were interrogated with R6G solutions over respective concentration ranges of 10^{-7} to 10^{-11} M for the ZnO: Cu/Ag structures and a significantly lower range of 10^{-10} to 10^{-14} M for the ZnO: Cu/FTO/Ag structures. The collected SERS spectra reveal a clear concentration-dependent response for both substrate types, with the characteristic Raman peaks systematically intensifying with increasing R6G concentration. Critically, the

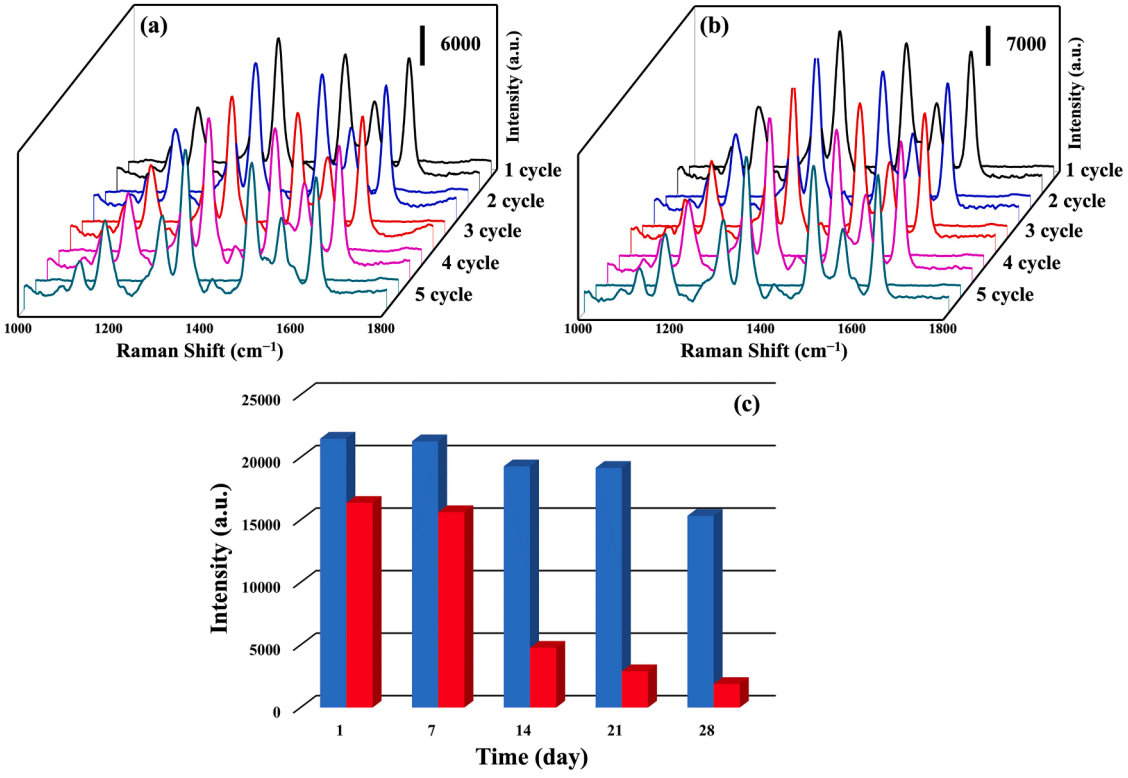


Fig. 10. Raman spectra of (10^{-6} M) R6G solution at the five cycles on (a) ZnO: Cu/Ag nano-heterostructure arrays and (b) ZnO: Cu/FTO/Ag nano-heterostructure arrays. (c) The SERS intensities of ZnO: Cu/Ag and ZnO: Cu/FTO/Ag nano-heterostructure arrays at 1648 cm^{-1} of R6G solution at designated time intervals.

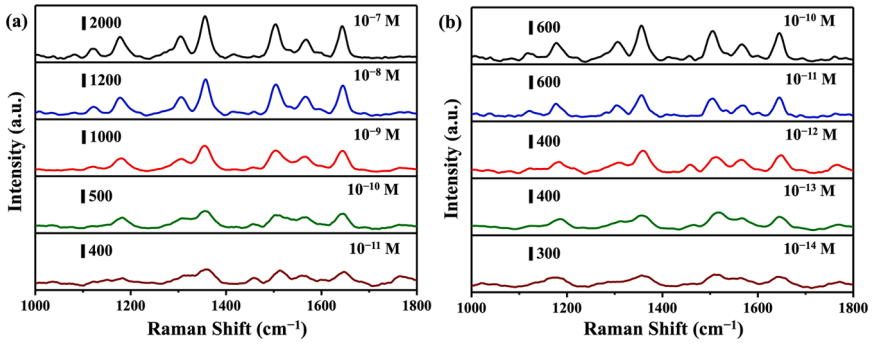


Fig. 11. The Raman spectra of (a) ZnO: Cu/Ag nano-heterostructure arrays and (b) ZnO: Cu/FTO/Ag nano-heterostructure arrays under the different concentrations of R6G solution.

incorporation of the FTO interlayer yielded a three-order-of-magnitude improvement in the limit of detection (LOD), reducing it from 10 pM (for ZnO: Cu/Ag) to an ultra-trace level of 1 fM. This substantial gain unequivocally confirms the superior analytical sensitivity of the fabricated ZnO: Cu/FTO/Ag nano-heterostructures.

To validate the practical utility and versatility of our fabricated ZnO: Cu/Ag and ZnO: Cu/FTO/Ag nano-heterostructures, their performance in the SERS detection of a key pharmaceutical compound was investigated. Amoxicillin, a commonly prescribed antibacterial drug, is widely used to treat bacterial infections in both humans and animals [66]. Fig. 12a and b display the concentration-dependent SERS spectra of amoxicillin acquired from the ZnO: Cu/Ag and ZnO: Cu/FTO/Ag nano-heterostructures, respectively, after a one-hour incubation. Specifically, concentrations ranging from 10^{-5} to 10^{-7} M were used to interrogate the ZnO: Cu/Ag structures, while the FTO-enhanced ZnO: Cu/FTO/Ag heterostructures were evaluated over a much lower range of 10^{-9} to 10^{-11} M. As observed in both figures, a clear concentration-dependent response was evident, with the signal intensities of characteristic amoxicillin peaks directly correlating with increasing analyte concentration. Remarkably, the ZnO: Cu/FTO/Ag nano-heterostructures enabled the clear identification of characteristic amoxicillin peaks at concentrations as low as 10 pM (10^{-11} M). Table S1 provides a comparative summary of previously reported SERS heterostructures used for detecting R6G and amoxicillin, revealing that most earlier systems exhibit relatively limited detection capability. In contrast, the picomolar-level response observed in this work clearly demonstrates the substantially enhanced sensitivity and ultralow LOD of the ZnO: Cu/FTO/Ag nano-heterostructures, highlighting the essential role of the FTO interlayer in interfacial charge-transfer–mediated enhancement. This pronounced improvement in analytical performance demonstrates the effectiveness of our structural design and further indicates that these substrates offer strong potential for rapid, trace-level monitoring of pharmaceutical residues, environmental contaminants, and other chemical targets.

To critically assess the pH-dependent performance and practical applicability of our SERS platform, its response was systematically evaluated over a range of pH values, a crucial parameter in real-world analytical scenarios. The SERS signal from a fixed concentration of amoxicillin (10^{-6} M) was investigated using both the ZnO: Cu/Ag and the previously optimized ZnO: Cu/FTO/Ag nano-heterostructure arrays. As shown in Fig. 13a and b, a clear pH-dependent trend was observed, with the optimal Raman enhancement being consistently achieved at a slightly acidic pH of 6 for both substrate types. This distinct pH optimum can be rationalized by considering the acid-base properties of amoxicillin. As an amphoteric molecule, amoxicillin possesses both a carboxylic acid group ($pK_a \approx 2.7$) and a primary amine group ($pK_a \approx 7.4$). Consequently, its speciation and net charge are highly sensitive to the solution's pH. At the optimal pH of 6, the carboxylic acid group is fully deprotonated ($-COO^-$) while the amine group remains predominantly protonated ($-NH_3^+$), resulting in a net zwitterionic state. It is postulated that this zwitterionic form facilitates optimal electrostatic interactions and adsorption orientation on the SERS substrate surface. This conformation likely brings key vibrational moieties into the closest proximity with the plasmonic 'hotspots' generated by the Ag nanoparticles, thereby maximizing the enhancement. This finding not only highlights the pH-sensitivity of the analyte-substrate interaction but also underscores the critical importance of pH buffering for achieving reliable sensitivity and reproducibility in practical SERS-based diagnostics.

To bridge the gap between idealized laboratory conditions and practical application, a critical investigation into the substrate's performance in realistic aqueous matrices was conducted. Specifically, amoxicillin (10^{-6} M) was spiked into three distinct water types representing a gradient of complexity: ultrapure deionized (DI) water (the ideal control), reverse osmosis (RO) water, and common tap water (the complex matrix). The SERS spectra acquired from substrates immersed in these solutions are presented in Fig. 14a and b. Analysis of the spectra

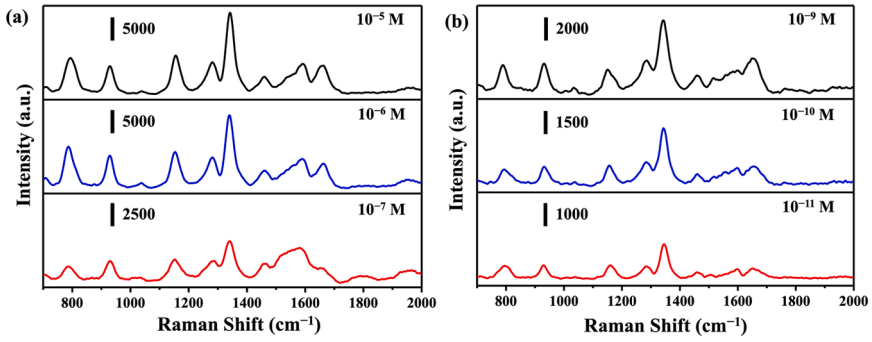


Fig. 12. The Raman spectra of (a) ZnO: Cu/Ag nano-heterostructure arrays and (b) ZnO: Cu/FTO/Ag nano-heterostructure arrays under the different concentrations of amoxicillin solution.

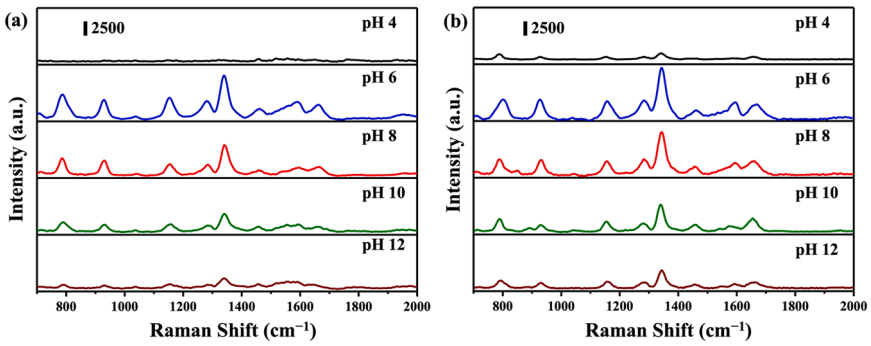


Fig. 13. The Raman spectra of (a) ZnO: Cu/Ag nano-heterostructure arrays and (b) ZnO: Cu/FTO/Ag nano-heterostructure arrays under the different pH values.

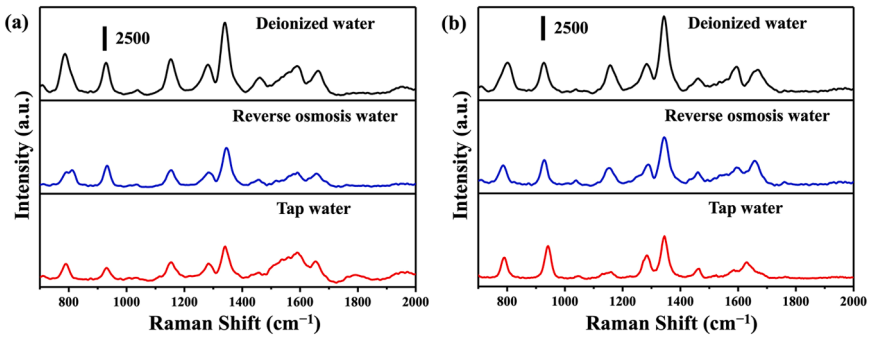


Fig. 14. The Raman spectra of (a) ZnO: Cu/Ag nano-heterostructure arrays and (b) ZnO: Cu/FTO/Ag nano-heterostructure arrays under different water media.

reveals a pronounced matrix-dependent effect: while the characteristic Raman peak positions for amoxicillin remained stable, their signal intensities were significantly attenuated in the more complex media. The most intense and unambiguous Raman enhancement was observed in the DI water control. This signal attenuation is attributed to the presence of competing interferents in the RO and tap water. In the case of tap water, a complex mixture of inorganic ions (e.g., Ca^{2+}, Mg^{2+}, and Cl^{-}) and natural organic matter can competitively adsorb onto the SERS substrate's active sites. This adsorption competition either physically blocks the amoxicillin molecules from reaching the plasmonic hotspots or alters the surface chemistry, thereby hindering efficient molecular adsorption and diminishing the SERS signal. Although the signal intensity decreased markedly in RO and tap water, the differences between these two non-ideal media were less pronounced, suggesting that even trace levels of impurities can significantly affect the sensor's performance. This result clearly highlights the critical influence of the sample matrix on SERS response. It highlights the need to develop robust calibration strategies or adequate sample pretreatment protocols to ensure reliable quantification in real-world analytical scenarios.

4. Conclusions

In conclusion, a novel 3D hierarchical SERS platform based on ZnO: Cu/FTO/Ag nano-heterostructures was successfully engineered via a scalable, synergistic fabrication strategy. This approach combined a facile wet-chemical synthesis of vertically aligned, [001]-oriented ZnO: Cu nanoneedle arrays with sequential RF (FTO) and DC (Ag) magnetron sputtering. The systematic investigation unequivocally demonstrated that the insertion of a 5.5 nm amorphous FTO interlayer is the critical design element responsible for the substrate's superior performance. This FTO layer was shown to induce a powerful dual-enhancement mechanism: (1) it facilitated interfacial charge transfer (ICT), providing a synergistic chemical enhancement, and (2) it amplified the electromagnetic enhancement, a finding corroborated by FDTD simulations, which showed the FTO layer narrows inter-particle gaps and advantageously redistributes the plasmonic field into these 'hotspot' junctions. This optimized architecture yielded an outstanding enhancement factor (EF) of 5.95×10^8, a 1.42-fold improvement over its ZnO: Cu/Ag counterpart. Beyond signal amplification, the FTO interlayer also imparted exceptional 21-day storage stability, likely acting as a protective barrier against Ag degradation. The substrate demonstrated excellent spatial uniformity and photocatalytic reusability. The practical utility of this design was validated by achieving an ultra-low limit of detection for Rhodamine 6 G (1 fM) and the antibiotic amoxicillin (10 pM). While performance is dependent on pH and complex matrices, highlighting the need for future optimization (e.g., surface functionalization), this work confirms that engineering such metal-insulator-semiconductor heterostructures is a highly effective strategy for enhancing performance. This study paves the way for the development of robust, ultra-sensitive, and stable SERS platforms for applications in environmental monitoring, pharmaceutical analysis, and point-of-care diagnostics.

CRediT authorship contribution statement

Tung-Hao Chang: Writing – original draft, Supervision, Resources, Project administration, Funding acquisition. **Yu-Fan Chen:** Validation, Investigation, Formal analysis, Data curation. **Yang-Chun Lee:** Software. **Yu-Cheng Chang:** Writing – review & editing, Writing – original draft, Visualization, Supervision, Software, Resources, Project administration, Methodology, Funding acquisition, Conceptualization.

Declaration of competing interest

The authors declare the following financial interests/personal relationships which may be considered as potential competing interests:

Yu-Cheng Chang reports financial support was provided by National Science and Technology Council. If there are other authors, they declare that they have no known competing financial interests or personal relationships that could have appeared to influence the work reported in

this paper.

Acknowledgments

The authors gratefully acknowledge the generous financial support from the National Science and Technology Council (NSTC) of Taiwan through grant nos. NSTC 112-2221-E-035-017-MY3 and NSTC 113-2221-E-035-023-MY3. This support was instrumental in the successful execution and completion of this research.

Supplementary materials

Supplementary material associated with this article can be found, in the online version, at doi:10.1016/j.surfin.2026.108930.

Data availability

Data will be made available on request.

References

[1] A. Campion, P. Kambhampati, Surface-enhanced Raman scattering, Chem. Soc. Rev. 27 (1998) 241–250.
[2] H. Ilkhani, T. Hughes, J. Li, C.J. Zhong, M. Hepel, Nanostructured SERS-electrochemical biosensors for testing of anticancer drug interactions with DNA, Biosens. Bioelectron. 80 (2016) 257–264.
[3] H. Ko, S. Singamaneni, V.V. Tsukruk, Nanostructured surfaces and assemblies as SERS Media, Small 4 (2008) 1576–1599.
[4] L.M. Almehmadi, I.K. Lednev, Surface-enhanced raman spectroscopy at the interface between drug discovery and personalized medicine, J. Phys. Chem. C 128 (2024) 18135–18143.
[5] R. Goel, S. Chakraborty, V. Awasthi, V. Bhardwaj, S.K. Dubey, Exploring the various aspects of Surface enhanced Raman spectroscopy (SERS) with focus on the recent progress: sERS-active substrate, SERS-instrumentation, SERS-application, Sens. Actuat. A: Phys. 376 (2024) 115555.
[6] S. Mahanty, S. Majumder, R. Paul, R. Boroujerdi, E. Valsami-Jones, C. Laforsch, A review on nanomaterial-based SERS substrates for sustainable agriculture, Sci. Total Environ. 950 (2024) 174252.
[7] M. Rycenga, C.M. Cobley, J. Zeng, W. Li, C.H. Moran, Q. Zhang, D. Qin, Y. Xia, Controlling the synthesis and assembly of silver nanostructures for plasmonic applications, Chem. Rev. 111 (2011) 3669–3712.
[8] M. Fan, G.F.S. Andrade, A.G. Brolo, A review on the fabrication of substrates for surface enhanced raman spectroscopy and their applications in analytical chemistry, Anal. Chim. Acta 693 (2011) 7–25.
[9] M. Liu, X. Hu, C. Zhang, M. Shafi, L. Ma, B. Lv, A. Rahim, M. Saleem, L. Zhao, Localized surface plasmon resonance enhanced charge transfer effect in MoO2/ZnSe nanocomposites enabling efficient SERS detection and visible light photocatalytic degradation, Sens. Actuat. B Chem. 398 (2024) 134688.
[10] M.E. Abdelsalam, P.N. Bartlett, J.J. Baumberg, S. Cintra, T.A. Kelf, A.E. Russell, Electrochemical SERS at a structured gold surface, Electrochem. Commun. 7 (2005) 740–744.
[11] C. Zhang, C. Li, J. Yu, S. Jiang, S. Xu, C. Yang, Y.J. Liu, X. Gao, A. Liu, B. Man, SERS activated platform with three-dimensional hot spots and tunable nanometer gap, Sens. Actuat. B Chem. 258 (2018) 163–171.
[12] L. Lu, A. Eychmüller, Ordered macroporous bimetallic nanostructures: design, characterization, and applications, Acc. Chem. Res. 41 (2008) 244–253.
[13] J.P. Camden, J.A. Dieringer, J. Zhao, R.P. Van Duyne, Controlled plasmonic nanostructures for surface-enhanced spectroscopy and sensing, Acc. Chem. Res. 41 (2008) 1653–1661.
[14] M.E. Stewart, C.R. Anderton, L.B. Thompson, J. Maria, S.K. Gray, J.A. Rogers, R. G. Nuzzo, Nanostructured plasmonic sensors, Chem. Rev. 108 (2008) 494–521.
[15] R. Chen, L. Jensen, Interpreting the chemical mechanism in SERS using a Raman bond model, J. Chem. Phys. 152 (2020) 024126.
[16] P. Karthick Kannan, P. Shankar, C. Blackman, C.-H. Chung, Recent advances in 2D inorganic nanomaterials for SERS sensing, Adv. Mater. 31 (2019) 1803432.
[17] C. Li, Y. Huang, X. Li, Y. Zhang, Q. Chen, Z. Ye, Z. Alqarni, S.E.J. Bell, Y. Xu, Towards practical and sustainable SERS: a review of recent developments in the construction of multifunctional enhancing substrates, J. Mater. Chem. C 9 (2021) 11517–11552.
[18] P.A. Mosier-Boss, Review of SERS substrates for chemical sensing, Nanomaterials (2017) 7.
[19] Z. Li, X. Huang, G. Lu, Recent developments of flexible and transparent SERS substrates, J. Mater. Chem. C 8 (2020) 3956–3969.
[20] J. Wu, Y. Du, C. Wang, S. Bai, T. Zhang, T. Chen, A. Hu, Reusable and long-life 3D Ag nanoparticles coated Si nanowire array as sensitive SERS substrate, Appl. Surf. Sci. 494 (2019) 583–590.
[21] T.-H. Chang, K.-W. Chuang, Y.-C. Chang, Ag/Ga-doped ZnO/pyramidal silicon as a multifunctional surface-enhanced Raman scattering substrate, J. Alloy. Compd. 893 (2022) 162288.
[22] Y. Liu, H. Ma, X.X. Han, B. Zhao, Metal–semiconductor heterostructures for surface-enhanced Raman scattering: synergistic contribution of plasmons and charge transfer, Mater. Horiz. 8 (2021) 370–382.
[23] S. Cong, X. Liu, Y. Jiang, W. Zhang, Z. Zhao, Surface enhanced Raman scattering revealed by interfacial charge-transfer transitions, Innovation 1 (2020) 100051.
[24] J. Lu, J. Yang, S.C. Singh, Z. Zhan, Z. Yu, W. Xin, T. Huang, C. Guo, Hierarchical micro/nanostructured TiO2/Ag substrates based on femtosecond laser structuring: a facile route for enhanced SERS performance and location predictability, Appl. Surf. Sci. 478 (2019) 737–743.
[25] C. Chen, X. Wang, Y. Zhang, X. Li, H. Gao, G.I.N. Waterhouse, X. Qiao, Z. Xu, A molecularly-imprinted SERS sensor based on a TiO2@Ag substrate for the selective capture and sensitive detection of tryptamine in foods, Food Chem. 394 (2022) 133536.
[26] T.-H. Chang, Y.-C. Chang, S.-H. Wu, Ag nanoparticles decorated ZnO: Al nanoneedles as a high-performance surface-enhanced Raman scattering substrate, J. Alloy. Compd. 843 (2020) 156044.
[27] Y.-C. Chang, Low temperature and large-scale growth of ZnO nanoneedle arrays with enhanced optical and surface-enhanced Raman scattering properties, Sens. Actuat. B Chem. 225 (2016) 498–503.
[28] N. Ge, X. Hu, Z. Pan, S. Cai, F. Fu, Z. Wang, J. Yao, X. Liu, Sustainable fabrication of cellulose aerogel embedded with ZnO@noble metal (Ag, Au, Ag-Au) NPs for sensitive and reusable SERS application, Colloids Surf. A Physicochem. Eng. Asp. 671 (2023) 131650.
[29] T.-H. Chang, Y.-C. Chang, C.-M. Chen, K.-W. Chuang, C.-M. Chou, A facile method to directly deposit the large-scale Ag nanoparticles on a silicon substrate for sensitive, uniform, reproducible and stable SERS substrate, J. Alloy. Compd. 782 (2019) 887–892.
[30] T.-H. Chang, K.-W. Chuang, Y.-C. Chang, C.-M. Chou, Optimizing and improving the growth of Ag nanoparticles decorated on the silicon pyramid for surface-enhanced raman spectroscopy, Mater. Chem. Phys. 280 (2022) 125823.
[31] L. Wu, W. Zhang, C. Liu, M.F. Foda, Y. Zhu, Strawberry-like SiO2/Ag nanocomposites immersed filter paper as SERS substrate for acrylamide detection, Food Chem. 328 (2020) 127106.
[32] W. Yin, L. Wu, F. Ding, Q. Li, P. Wang, J. Li, Z. Lu, H. Han, Surface-imprinted SiO2@Ag nanoparticles for the selective detection of BPA using surface enhanced raman scattering, Sens. Actuat. B Chem. 258 (2018) 566–573.
[33] T. Wang, Z. Zhang, F. Liao, Q. Cai, Y. Li, S.-T. Lee, M. Shao, The effect of dielectric constants on noble metal/semiconductor SERS enhancement: FDTD simulation and experiment validation of Ag/Ge and Ag/Si substrates, Sci. Rep. 4 (2014) 4052.
[34] J. Huang, F. Chen, Q. Zhang, Y. Zhan, D. Ma, K. Xu, Y. Zhao, 3D Silver nanoparticles decorated zinc oxide/silicon heterostructured nanomace arrays as high-performance surface-enhanced raman scattering substrates, ACS Appl. Mater. Interface. 7 (2015) 5725–5735.
[35] J. Liu, G. Meng, Z. Li, Z. Huang, X. Li, Ag-NP@Ge-nanotaper/Si-micropillar ordered arrays as ultrasensitive and uniform surface enhanced raman scattering substrates, Nanoscale 7 (2015) 18218–18224.
[36] A. Rezaei, M.R. Rezaei, M.H. Sayadi, 3D network structure graphene hydrogel-Fe3O4@SnO2/Ag via an adsorption/photocatalysis synergy for removal of 2,4 dichlorophenol, J. Taiwan Inst. Chem. Eng. 121 (2021) 154–167.
[37] D. Yang, R. Yang, S. Priya, S. Liu, Recent advances in flexible perovskite solar cells: fabrication and applications, Angew. Chem. Int. Ed. 58 (2019) 4466–4483.
[38] J. Theerthagiri, A.R. Senthil, J. Madhavan, T. Maiyalagan, Recent progress in non-platinum counter electrode materials for dye-sensitized solar cells, ChemElectroChem 2 (2015) 928–945.
[39] Z. Chen, D. Pan, Z. Li, Z. Jiao, M. Wu, C.-H. Shek, C.M.L. Wu, J.K.L. Lai, Recent advances in tin dioxide materials: some developments in thin films, nanowires, and nanorods, Chem. Rev. 114 (2014) 7442–7486.
[40] C. Yu-Cheng, L. Yu-Wen, MoS2@SnO2 core-shell sub-microspheres for high efficient visible-light photodegradation and photocatalytic hydrogen production, Mater. Res. Bull. 129 (2020) 110912.
[41] J.P. Cheng, J. Wang, Q.Q. Li, H.G. Liu, Y. Li, A review of recent developments in tin dioxide composites for gas sensing application, J. Indust. Eng. Chem. 44 (2016) 1–22.
[42] J. Wu, Y. Zhang, J. Zhou, K. Wang, Y.-Z. Zheng, X. Tao, Uniformly assembling n-type metal oxide nanostructures (TiO2 nanoparticles and SnO2 nanowires) onto P doped g-C3N4 nanosheets for efficient photocatalytic water splitting, Appl. Catal., B 278 (2020) 119301.
[43] A. Korjenic, K.S. Raja, Electrochemical stability of fluorine doped tin oxide (FTO) coating at different pH conditions, J. Electrochem. Soc. 166 (2019) C169–C184.
[44] G. Genesio, J. Maynadié, M. Carboni, D. Meyer, Recent status on MOF thin films on transparent conductive oxides substrates (ITO or FTO), New J. Chem. 42 (2018) 2351–2363.
[45] G. Divyapriya, P. Thangadurai, I. Nambi, Green approach to produce a graphene thin film on a conductive LCD matrix for the oxidative transformation of ciprofloxacin, ACS Sustain. Chem. Eng. 6 (2018) 3453–3462.
[46] D. Saikia, R. Sarma, Organic light-emitting diodes with a perylene interlayer between the electrode–Organic interface, J. Electron. Mater. 47 (2018) 737–743.
[47] C. Hora, F. Santos, A.M.V.M. Pereira, M.G.F. Sales, D. Ivanou, A. Mendes, PEDOT-graphene counter-electrode for solar and improved artificial light conversion in regular, bifacial and FTO-less cobalt mediated DSSCs, Electrochim. Acta 412 (2022) 140140.
[48] H.M. Asif Javed, A.A. Qureshi, R. Mehmood, M.I. Tahir, S. Javed, M. Sarfaraz, M. Y. Javaid, M. Awais, U. Ali, Hydrogen treated TiO2 nanoparticles onto FTO glass as photoanode for dye-sensitized solar cells with remarkably enhanced performance, Int. J. Hydrog. Energy 46 (2021) 14311–14321.

[49] K. Guo, J. Ding, Z. Han, J. Liu, X. Yang, P. Hu, Y. Jiao, F. Teng, Construction a quasi-solid-state photoelectrochemical type photodetector based on WO3/PVA/ZnSO4 and its application in near ultraviolet light detection, Surf. Interfac. 49 (2024) 104422.
[50] Z. Wang, Y. Liu, F. Zhao, W. Yang, S. Deng, C. Li, J. Cao, W. An, J. Pan, L. Shi, The rapid thermal annealing in hole transition layer amelioration for enhancing large-area perovskite solar cell via potential regulation and hole induction, Appl. Phys. Lett. 127 (2025).
[51] J. Zhang, Z. Liu, J. Wang, Y. Zhang, J. Dong, J. Gao, L. Zhang, J. Wang, P. Tang, Q. Zhang, 3D Coaxially printing rGO aerogel-based biocompatible Fiber for peripheral nerve regeneration, Adv. Fiber Mater. 6 (2024) 713–726.
[52] P. Hong, L. Wu, X. Shi, P. Hu, H. Fan, F. Teng, Influence of buffer layer on the performance of ZnO film based photoconductive detectors, J. Appl. Phys. 138 (2025).
[53] D. Wang, R. Wang, C. Jia, B. He, J. Cao, W. An, L. Shi, J. Pan, S. Deng, C. Li, Transparent CuGaO2/BaTiO3 nanoarray pn junction with high-entropy perovskite quantum dots for enhanced photoelectric response, Appl. Phys. Lett. 127 (2025).
[54] L.T. Tuyen, S.-R. Jian, N.T. Tien, P.H. Le, Nanomechanical and material properties of fluorine-doped tin oxide thin films prepared by ultrasonic spray pyrolysis: effects of F-doping, Mater. (Basel) (2019) 12.
[55] M. Althumayri, R. Das, R. Banavath, L. Beker, A.M. Achim, H.C. Koydemir, Recent advances in transparent electrodes and their multimodal sensing applications, Adv. Sci. 11 (2024) 2405099.
[56] Y.-C. Chang, C.-C. Hsu, S.-H. Wu, K.-W. Chuang, Y.-F. Chen, Fabrication of Cu-doped ZnO nanoneedles on different substrate via wet chemical approach: structural characterization and photocatalytic performance, Appl. Surf. Sci. 447 (2018) 213–221.
[57] E. Fabbretti, A.H. Husien, R. Patidar, K. Valadez-Villalobos, J. McGettrick, A. Amighini Alerhush, E. Parvazian, M.L. Davies, T. Watson, A. Minotto, G. Tseberlidis, A. Sassella, V. Trifiletti, S. Binetti, Enhancing the stability of inverted perovskite solar cells through Cu2ZnSnS4 nanoparticles hole transporting material, Sustain. Energy Fuels 9 (2025) 1486–1497.
[58] S. Brahma, Y.-W. Yeh, J.-L. Huang, C.-P. Liu, Cu-doped p-type ZnO nanostructures as unique acetone sensor at room temperature (~25 °C), Appl. Surf. Sci. 564 (2021) 150351.
[59] Z. Wan, Z. Li, J. Wang, S. Guo, H. Zhang, W. Chen, C. Li, H. Ding, Dual-function UiO-66/AgNPs/TiO2 SERS substrate with photocatalytic self-cleaning for recyclable detection of thiram, Surf. Interfac. 75 (2025) 107765.
[60] R. Sharma, A. Dhillon, D. Kumar, Mentha-stabilized silver nanoparticles for high-performance colorimetric detection of Al(III) in aqueous systems, Sci. Rep. 8 (2018) 5189.
[61] V. Eskandari, H. Sahbafar, L. Zeinalizad, F. Sabzian-Molaei, M.H. Abbas, A. Hadi, A surface-enhanced Raman scattering (SERS) biosensor fabricated using the electrodeposition method for ultrasensitive detection of amino acid histidine, J. Mol. Struct. 1274 (2023) 134497.
[62] M. Shafi, P. Duan, W. Liu, W. Zhang, C. Zhang, X. Hu, C. Liu, S. Wali, S. Jiang, C. Zhang, B. Man, M. Liu, Recyclable surface-enhanced Raman spectroscopy (SERS) platform fabricated with Ag-decorated ZnSe nanowires and metamaterial, Sens. Actuat. B Chem. 380 (2023) 133410.
[63] S. Li, N. Zhang, N. Zhang, D. Lin, X. Hu, X. Yang, Three-dimensional ordered Ag/ZnO/Si hierarchical nanoflower arrays for spatially uniform and ultrasensitive SERS detection, Sens. Actuat. B Chem. 321 (2020) 128519.
[64] T.T.T. Le, T.H. Bui, H.P. Le, T.G.A. Pham, T.T.H. Pham, C.D. Truong, L. Lieu, Hybrid nanomaterials based on ZnO/WO3 and rGO for enhanced photocatalytic degradation and SERS detection applications, Appl. Surf. Sci. 700 (2025) 163253.
[65] Q.-D. Mai, D. Thi Hanh Trang, T. Ngoc Bach, V. Thi Le Na, A.-T. Pham, A.-T. Le, Synergizing PIERS and photocatalysis effects in a photo-responsive Ag/TiO2 nanostructure for an ultrasensitive and renewable PI-PC SERS technique, RSC Adv 15 (2025) 4149–4162.
[66] Y.-C. Chang, S.-H. Wu, Bi-functional Al-doped ZnO@SnO2 heteronanowires as efficient substrates for improving photocatalytic and SERS performance, J. Ind. Eng. Chem. 76 (2019) 333–343.